PTI Journal *Technical Paper*

CORNER POST-TENSIONED SLAB-COLUMN CONNECTIONS

By

THOMAS H.-K. KANG AND YU HUANG

POST-TENSIONING INSTITUTE ®

Authorized reprint from: AUGUST 2013 issue of the PTI Journal

CORNER POST-TENSIONED SLAB-COLUMN CONNECTIONS

BY THOMAS H.-K. KANG AND YU HUANG

The behavior of corner post-tensioned (PT) slab-column connections was rarely studied. This study performs in-depth research for better understanding complicated moment and shear-transfer mechanism at corner PT slab-column connections. Literature was reviewed and discussion was made on the previous experimental study, which led to carrying out sophisticated finite element simulations of previously tested, two isolated-corner PT connections. The documented test results, along with the finite element simulations, provide an innovative way to review the scarce test data in detail. Moreover, ACI 318 punching shear provisions were assessed using such a unique approach. The assessment shows that the current ACI 318 code is conservative in the punching shear design of corner PT slab-column connections.

KEYWORDS

Corner slab-column connections; finite element modeling; post-tensioned concrete; punching shear failure; unbonded tendons.

INTRODUCTION

Prestressed concrete is essential in many applications today to fully use concrete compressive strength and—through proper design—to control cracking and deflection. Although design methods have been developed over the decades, an understanding of the ultimate mechanism in the prestressed concrete system is still greatly needed in many aspects. Such aspects include the intricate problems of punching shear failure of a post-tensioned (PT) two-way slab system. However, to perform extensive experimental tests on each subject is extremely expensive and time-consuming. The finite element method, on the other hand, was introduced into structural analysis in the late 1960s. The efforts and developments made by many pioneering researchers over the past five decades have enabled the finite element method to become a versatile and powerful approach in structural analysis. The principal goals of this study are to develop modeling schemes for corner PT slab-column connections based on general-purpose finite element packages and evaluate the current building code regarding the corner PT connections.

RESEARCH SIGNIFICANCE

Little research has been conducted on corner PT slab-column connections. Previous multi-panel tests (Scordelis et al. 1959; Gamble 1964; Brotchie and Beresford 1967; Odello and Mehta 1967; Muspratt 1969; Burns and Hemakom 1977; Kosut et al. 1985; Burns and Hemakom 1985) included one to four corner connections in each of the specimens; however, the research was mainly focused on the flexural behavior of PT flat-plate systems and no specific study was conducted on the punching shear behavior of corner PT connections. In the 1990s, Moehle et al. (1994) conducted a biaxial cyclic test of two isolated-corner PT connections, and Garnder and Kallage (1998) conducted an ultimate load test of a four-panel PT flat plate with one interior and four corner connections. In the current analytical study, crucial data from the former (Moehle et al. 1994; Martinez-Cruzado 1993) were used to assess the behavior of corner PT connections in depth. The latter was also reviewed in the aspect of corner PT connections.

SUMMARY OF EXPERIMENTAL STUDY BY GARDNER AND KALLAGE (1998)

A two-bay by two-bay unbonded PT flat plate with four continuous panels was designed and tested by Gardner and Kallage (1998). The flat plate had a footprint of 19 ft 10-3/4 in. x 19 ft 10-3/4 in. (6.1 m x 6.1 m) with

PTI JOURNAL, V. 9, No. 1, August 2013. Received and reviewed under Institute journal publication policies. Pertinent discussion will be published in the next issue of *PTI JOURNAL* if received within 3 months of the publication.

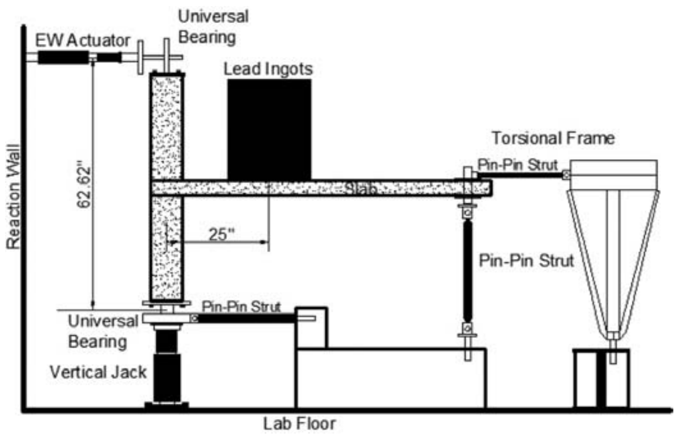

Fig. 1—Schematic view of test setup.

a center-to-center span length of 9 ft 11-7/8 in. (3.0 m) in each direction. The thickness of the slab was 3.54 in. (90 mm), which was supported by nine columns: one square interior column, two square edge columns, two round edge columns, two square corner columns, and two round corner columns. The PT tendons were draped in both directions, banded within the column strip in the east-west (E-W) direction and uniformly distributed in the north-south (N-S) direction. A downward load was uniformly distributed on top of the slab via 40 steel threaded rods. Gardner and Kallage (1998) intended to investigate punching shear behavior of PT slab-column connections without an isolated boundary condition. Due to a pump leaking failure, testing was aborted before punching shear failure occurred. The slab was repaired and shored thereafter to continue the test. Edge connections failed first in the subsequent tests. After shoring the failed connections, the slab was reloaded until punching failure of the interior column occurred. One corner connection failed after shoring the failed edge and interior connections. Gardner and Kallage (1998) claimed that the most reliable experimental data were obtained for the edge connection, whereas the actual experimental failure load could be larger for the interior and corner connections as the slab was degraded from the previous failure. Even with the previous damage, the measured strengths of edge and corner connections were larger than the calculated punching shear strengths without prestress. The precompression f_{pc} was reportedly effective and thus can be considered in calculating the punching shear capacity of edge and corner PT slab-column connections. For more detailed information about this experimental investigation, refer to Gardner and Kallage (1998).

EXPERIMENTAL PROGRAM (MOEHLE ET AL. 1994)

Moehle et al. (1994) investigated two 3/7-scale isolated-corner PT connections (Fig. 1). The slabs with the corner connection had an overall length of 7 ft 1-1/2 in. (2.2 m) in each direction and 3-5/8 in. (92 mm) in thickness. The corner connection was in the southwest corner, whereas other corners of the slab were supported by pin connections simulating an inflection boundary in the prototype structure. The slab with the edge connection had an overall length of 6 ft 11-11/32 in. (2.1 m) in both directions and a slab thickness of 3-5/8 in. (92 mm). Additional dead loads were applied to the slab before testing to achieve the desired gravity load in the column at the initialization of the test. Biaxial lateral loading was applied to the column top with several cycles of different drift ratios for the purpose of simulating multidirectional seismic loading. One of the conclusions reached in the experimental study was that the presence of high compressive stress in the slab-column connection region increases the shear strength of the connection. The increase of tensile stress was very small in the prestressing strand under constant gravity and increased lateral load.

Specimens C1 and C2 have identical geometry and reinforcement, whereas the only discrepancy between two specimens is different test procedures. The following descriptions are based on Specimen C1. Five 3/8 in. (10 mm) diameter prestressing strands were banded in the N-S direction concentrating at the column strip while prestressing strands were distributed along the E-W direction. All prestressing strands were inserted into flexible polyvinyl chloride (PVC) tubes to maintain an unbonded interface between the strand and the concrete. All prestressing strands were drape-shaped. Mild steel bars were provided only at the negative-moment region around the column. Details of dimensions and reinforcement are depicted in Fig. 2, with greater details available in the thesis of Martinez-Cruzado (1993).

Columns were designed to stay in the elastic range even under the largest lateral load. The half-story column below the slab was pinned at its end by a universal bearing and a vertical jack was installed under the universal bearing to adjust the gravity load during testing (Fig. 1). Another half-story column above the slab was pinned at an additional universal bearing, which connects to two actuators at N-S and E-W directions, respectively. Slabs were pinned at three corners by vertical struts other than the location of the column to simulate the boundary condition at inflection points. A torsional restraint frame was installed parallel to the N-S direction to minimize the slab in-plane torsion when the lateral loading was carried out. Several lead ingots were placed at calculated positions to simulate the required gravity load at initial. A cloverleaf displacement loading pattern was applied to the column top with several drift ratio cycles to simulate the seismic loading. Experimental design drift ratios of 0.1, 0.2, 0.5, 1.0, 1.5, and 3.0% were used for C1, and 0.2, 0.4, 0.8, 1.6, and 3.2% were applied to C2.

NUMERICAL MODELS

The modeling schemes used are the same as in the previously published PTI *JOURNAL* paper (Kang and Huang 2012) and elsewhere (Huang et al. 2010; Huang 2012). Although experiments involved a cloverleaf cyclic loading pattern for both C1 and C2, the numerical study only duplicates the first two steps of certain cycles—that is, applying a displacement loading at the column top toward the south first, then changing the loading direction to the west (Fig. 3). The drift ratios chosen for the numerical simulation were based on the response of lateral reaction versus drift ratio plots in the experiment, as shown in Fig. 3. Possible punching shear failures occurred during the selected drift ratio loading processes. The actual drift ratios recorded in the experiments are slightly different from the experimental design drift ratio. Besides Specimens C1 and C2, two additional imaginary Specimens C1-2.5 and C2-2.5 were introduced in the simulation purely based on the numerical nature. They are exactly the same as C1 and C2, except the ingot weight applied on them is 2.5 times of that in the experiment. The motivation of introducing two imaginary specimens is investigating shear redistribution along the critical section under larger gravity shear. There are two sets of analyses with different drift ratios for each specimen. Therefore, four specimens were modeled and eight simulations were carried out.

The effective prestress f_{se} used in the finite element analysis was determined from measured tendon force at the experiment. Prestress force was measured from the load cell located at the end of each tendon. The desired effective prestress level was achieved by several iterations of preliminary analyses via uniformly reducing the temperature field of the tendon. Before lateral load analysis, three initial analysis steps were performed which were, in order, the prestressing step, self-weight step, and ingot-weight step. Prestressing was exerted by constraining only the column top and bottom because the test specimens were

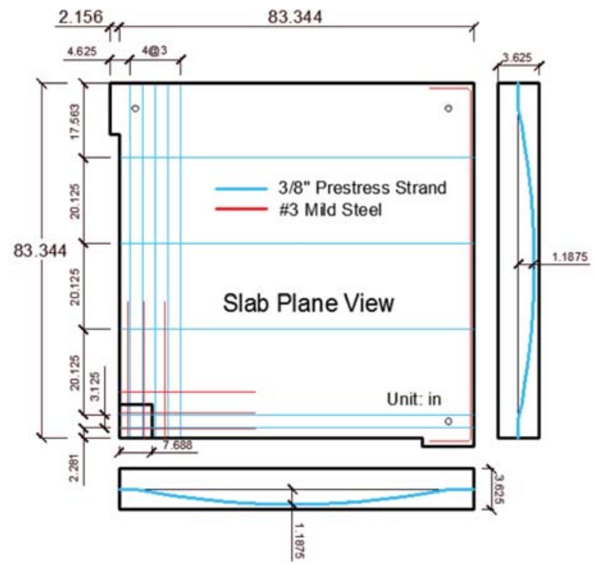

Fig. 2—Details of reinforcement and dimensions of Specimens C1 and C2. (Note: 1 ft = 305 mm; 1 in. = 25.4 mm.)

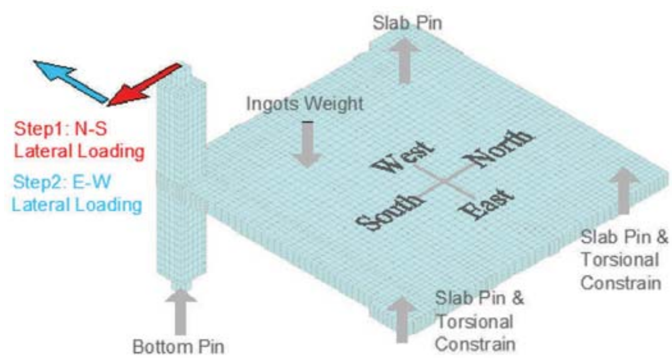

Specimens	c1a	c1a-2.5	c1b	c1b-2.5	c2a	c2a-2.5	c2b	c2b-2.5
N-S drift (%)	1.17	1.17	3.4	3.4	1.63	1.63	3.22	3.22
E-W drift (%)	1.35	1.35	3.58	3.58	1.48	1.48	3.24	3.24

Fig. 3—Drift ratios for different numerical simulations.

not constrained during their prestressing. Following the prestressing step, slab corners were immediately constrained as pin connections, as in the experiment, to be ready to sustain self-weight and ingot weight in subsequent steps. The lateral load analysis steps were initiated after applying the ingot-weight step, which ensures both the numerical and experimental conditions are as similar as possible.

NUMERICAL RESULTS AND VALIDATIONS

Lateral load versus drift ratio and damage pattern

Plots of lateral load versus drift ratio from C1 and C2 are first compared to the experimental data. Some differ-

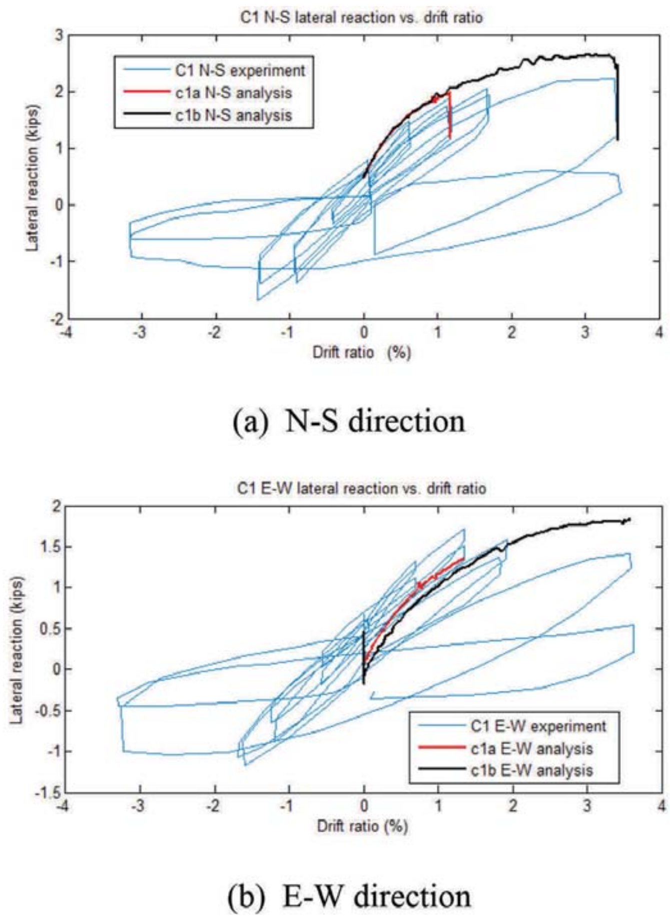

Fig. 4—Global responses of numerical simulations related to C1. (Note: 1 k = 4.45 kN.)

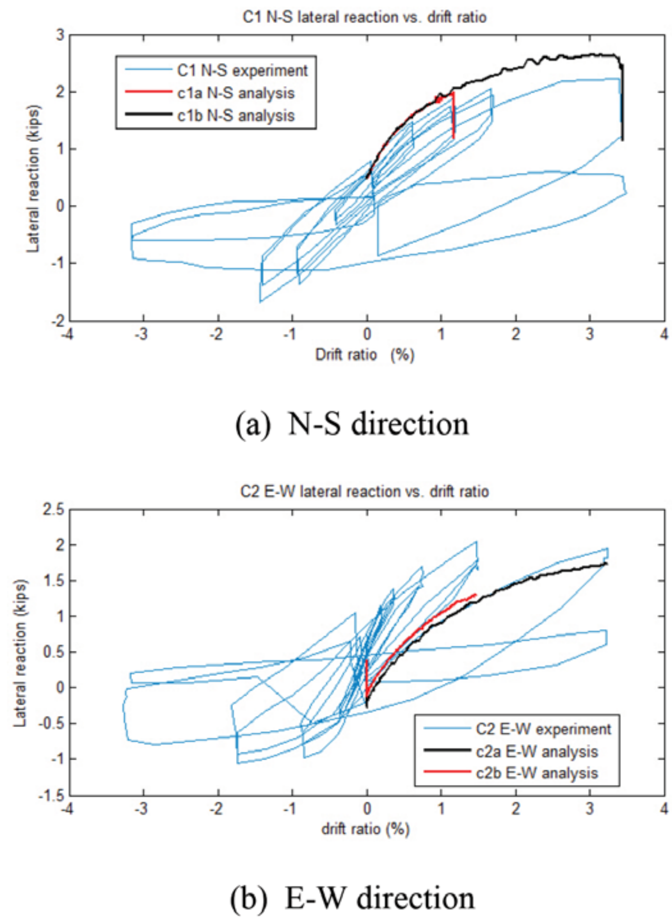

Fig. 5—Global responses of numerical simulations related to C2.

ences exist in loading conditions between experiments and analyses (cyclic versus monotonic). The original tests employed cloverleaf displacement loading patterns with several cycles of different drift ratios. Each cycle contains several steps to simulate cyclic loading conditions, which begin with N-S displacement loading followed by E-W displacement loading. These first two steps were selected in finite element analyses as monotonically increasing loadings. The discrepancy is that the experiments involved unloading for each cycle and the specimens could be damaged after one cycle of the test. The initial damage caused by the previous cycle, however, was not considered in the analyses. Every numerical simulation was performed without initial imperfection. Although these differences were present, a reasonable agreement between the experiment and numerical model is expected if finite element models are well-developed. Generally, in this case, numerical results at the N-S loading stage are expected to comply with the backbone curves of experiments, while this is not true at the E-W loading stage. The reason is that the initial E-W lateral reaction at each drift ratio cycle is different at the E-W loading stage. The aforementioned backbone comparison is not justified for the E-W loading stages. Alternatively, a reasonable agreement of the E-W lateral reaction at the end of this loading stage is expected instead.

Figure 4 shows the N-S and E-W lateral reactions at the N-S and E-W lateral loading stages respective of c1a and c1b. The numerical results reasonably agreed with experiments at the N-S lateral loading stage. However, c1a predicted a lower lateral reaction, while c1b predicted a higher lateral reaction at the end of the E-W lateral loading stage. Figure 5 shows the N-S and E-W lateral reactions at the N-S and E-W lateral loading stages respective of c2a and c2b. Except for c2a, which underestimated lateral reaction at the end of the E-W lateral loading stage, the rest of the models have good agreement with the experiments. Specimens C1 and C2 have identical geometry, are reinforced with similar prestressing strands, and have similar material properties, but C1 has initial damage caused by mishandling (cracks were found on the top surface at an angle of approximately 45 degrees with respect to the slab free edge). In addition, C1 has been tested with 11 repetitive cycles of cloverleaf loading. C1 could be severely damaged during tests, which might be another reason why larger discrepancies were found at the E-W lateral reaction plots. In contrast, C2, with only five cycles of cloverleaf loading and without initial damage, had less differences compared to numerical results.

The damage patterns of the simulation c1b and its experimental counterpart are shown in Fig. 6 and 7. It is noted that the numerical simulations showed much less damages than experimental observations. Several cycles of loading and unloading might have caused the excessive damage in the experiments. The idealized numerical boundary condition of the complicated experimental setup might also have caused the observed difference.

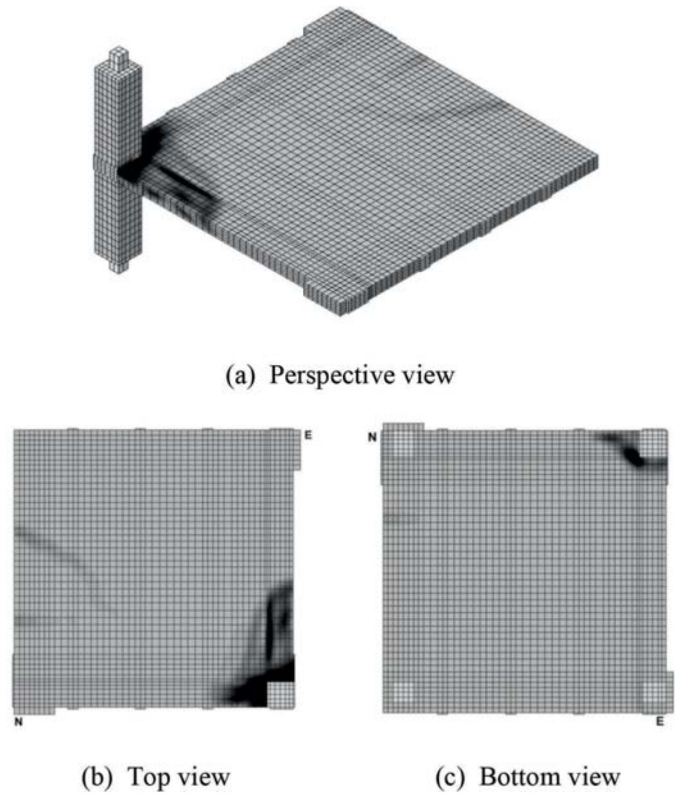

Fig. 6—Damage pattern of simulation c1b.

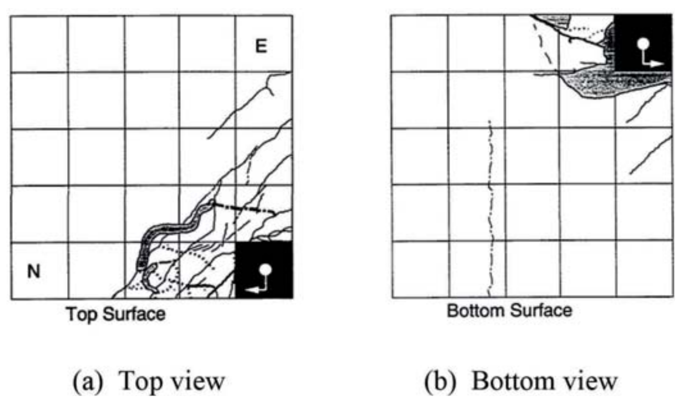

Fig. 7—Damage pattern of C1 (adapted from Martinez-Cruzado 1993).

Shear distribution along critical section

ACI 318-11, Section 11.11, (ACI Committee 318 2011) describes the moment and shear-transfer mechanism at slab-column connections. The total shear at the critical section is assumed to be the sum of direct shear and eccentric shear due to a fraction of unbalanced moment transfer. To study the shear-stress distribution under varied direct shear load and unbalanced moment, the shear-stress distribution along the critical section is plotted based on the numerical results. The "vertical" shear-stress distribution along the slab thickness direction is not addressed in the eccentric shear-stress model, which assumes the shear stress is independent of vertical position. To comply with this assumption and obtain the general pattern of the shear-stress distribution along the critical section, numerical shear stresses were extracted from the integration points of five vertical elements, which are in the same location on the plan view. Shear stresses τ_{12} and τ_{23} were read from the east and north faces of the critical section, respectively. The average of the five layers' shear stresses is plotted at eight locations on the east and north sides of the critical section (Fig. 8).

Figure 9 shows the shear-stress histories of each location at the critical section of the c1a analysis. The numerical shear stresses are plotted versus drift ratio, which clearly presents variations of the shear stresses during lateral loadings. The shear-stress histories calculated from the eccentric shear-stress model at Locations 1 (south corner on east face), 8 (front corner on east face), 9 (front corner on north face), and 16 (west corner on north face) are also included in Fig. 9 for comparison. It is obvious that the numerical shear stress trend at the south corner reasonably agrees with the calculation from the eccentric shear-stress model. However, a large difference of the initial shear stress is noticed at the south corner. This is because the eccentric shear-stress model only considers the direct shear and the unbalanced moment-induced eccentric shear at initial, while for this case, initial shear stress due

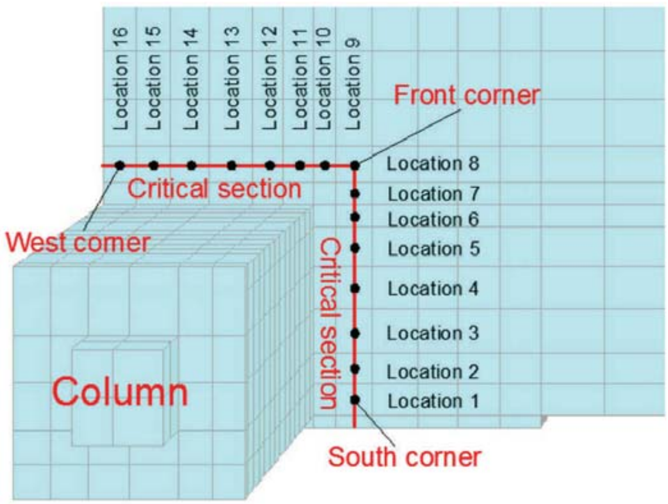

Fig. 8—Plan configuration for shear-critical section of corner PT slab-column connection.

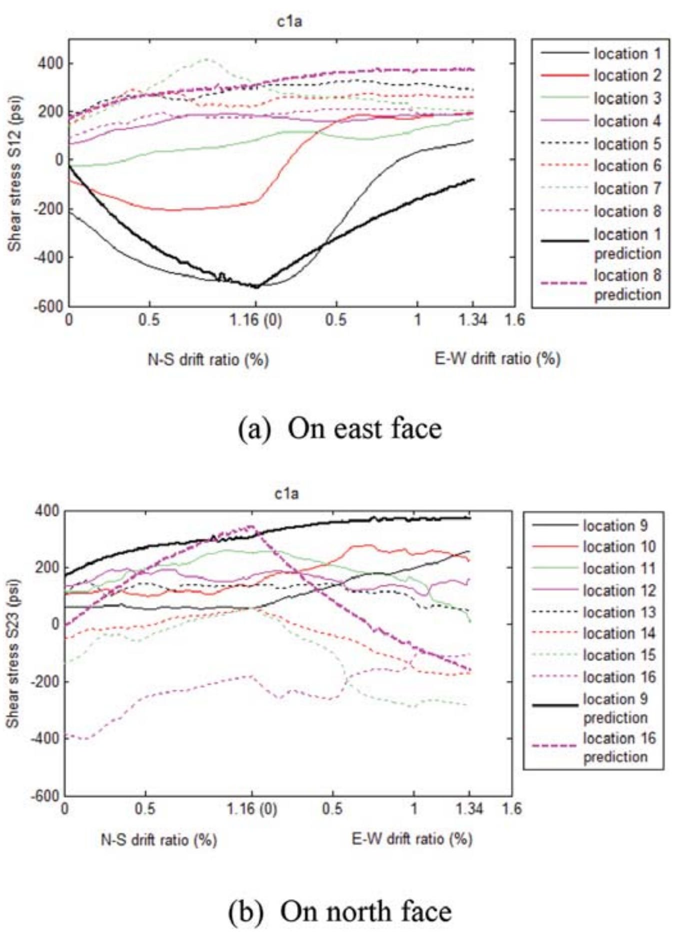

Fig. 9—Shear-stress histories at several points from simulation c1a. (Note: 1 psi = 6.89 kPa.)

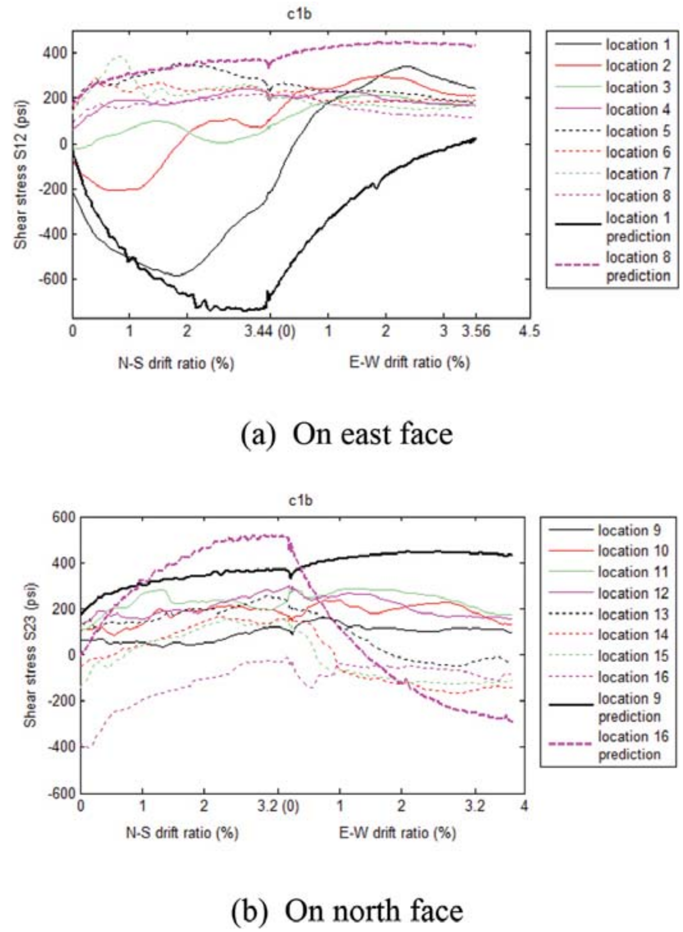

Fig. 10—Shear-stress histories at several points from simulation c1b. (Note: 1 psi = 6.89 kPa.)

to prestress is considerable. Given the fact that tendons are banded in the N-S direction concentrated on the column strip, the upward initial shear stress due to prestress at the north face of the critical section is much higher than that at the east face. As a result, the eccentric shear-stress model presents quite a different value than the numerical one. In spite of the different initial shear stresses, the trend of the shear-stress variation of numerical results and the eccentric shear-stress model predictions are similar. The shear-transfer mechanism described by the eccentric shear-stress model seems to be reasonable.

Figure 10 shows the same content for the c1b simulation. The stress at the front corner is much smaller than the eccentric shear-stress model prediction during the whole simulation, which might imply a smaller unbalanced moment-transfer ratio (more discussions about unbalanced moment transfer will be presented in the following section). The numerical results at both the south and west corners present similar patterns to the c1a simulation.

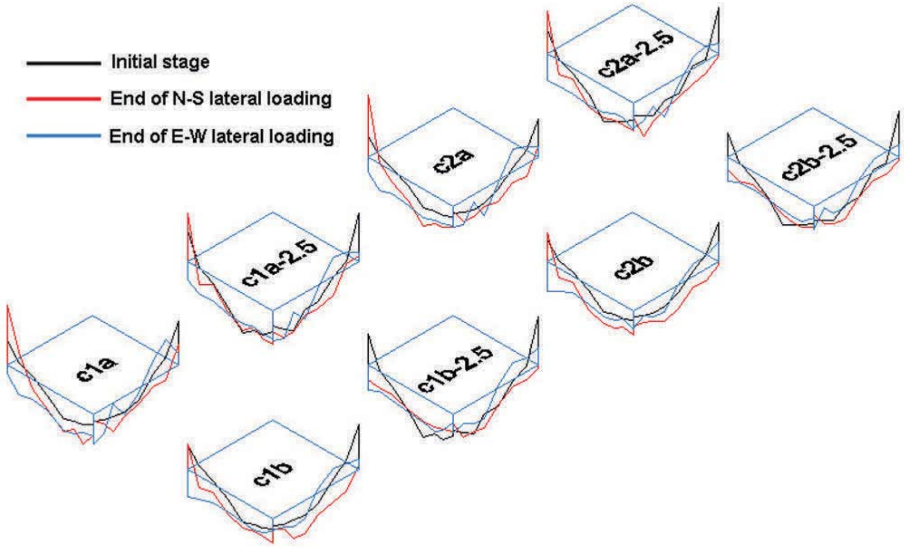

Fig. 11—Three-dimensional plots of shear-stress distribution of all simulations.

Numerical shear-stress distributions of all rest analyses (Huang 2012) behave similarly to c1a and c1b, which yield the conclusions as follows: 1) the eccentric shear-stress model predicts the shear-stress transfer and distribution trend reasonably well; 2) the shear stress calculated using the eccentric shear-stress model could differ greatly from the real case because of a presence of the large initial shear stress due to prestress and because of the following reason; and 3) a reduction of the unbalanced moment-transfer ratio might be considered in the calculation when the slab-column connection is cracked.

Figure 11 shows a three-dimensional plot of shear-stress distribution along the critical section of each analysis. Only the shear-stress distribution at the initial and end stages of N-S lateral loading and E-W lateral loading are shown in this figure. The relatively linear distributions of shear stresses are shown along the north and east face of the critical section, supporting the conclusion that the eccentric shear-stress model is reasonable and effective for corner PT slab-column connections.

ACI 318 CODE PROVISIONS FOR PUNCHING SHEAR

In this section, the description of the eccentric shear-stress model is first presented; then, the approach of calculating the design shear stress is introduced. Equations are evaluated associated with numerical simulations and experiments. Further analyses based on comparisons among the design shear stress, numerical shear stress, and ACI 318 permitted shear-stress capacity are presented in this section, which yields suggestions to the currently adopted eccentric shear-stress model in the code. The adjustment of unbalanced moment transfer factor γ_f is not permitted for prestressed slab-column connections according to ACI 318-11, Section 13.5.3.3 (ACI Committee 318 2011). The prestressing effect is not taken into account when calculating the shear capacity of such corner connections according to ACI 318-11, Section 11.11.2.2. To evaluate these provisions, the numerical shear stresses obtained along the critical section will be used as shown in the following subsections. Note that such stress values and distributions have not been obtained directly from most experiments of two-way slabs and slab-column connections.

Evaluation of eccentric shear-stress model

The current building code (ACI 318-11) presents a model dealing with unbalanced moment shear transfer at slab-column connections. A portion of unbalanced moment is assumed to be transferred by flexure, while the rest is transferred by the eccentric shear. The fractions of unbalanced moment transferred by flexure and eccentric shear at a corner PT connection are given by γ_f and γ_v, respectively—as per ACI 318-11, Sections 13.5.3.2 and 11.11.7.1—and as shown by the following equations

$$\gamma_x = 1 - \frac{1}{1 + \frac{2}{3}\sqrt{\frac{c_y + d/2}{c_x + d/2}}} \tag{1}$$

$$\gamma_y = 1 - \frac{1}{1 + \frac{2}{3}\sqrt{\frac{c_x + d/2}{c_y + d/2}}} \tag{2}$$

where d is the effective depth of the slab; and c_x and c_y are the column dimensions in parallel with and perpendicular to the considered unbalanced moment, respectively. The design shear stress at each corner of the critical section for a corner connection is determined as follows

$$v_{u(A)} = \frac{V_u}{A_c} + \frac{\gamma_x\left(M_{u,y} - V_u g_1\right)c_{AB}}{J_{cy}} + \frac{\gamma_y\left(M_{u,x} - V_u g_2\right)c_{AD}}{J_{cx}} \tag{3}$$

$$v_{u(D)} = \frac{V_u}{A_c} + \frac{\gamma_x\left(M_{u,y} - V_u g_1\right)c_{AB}}{J_{cy}} - \frac{\gamma_y\left(M_{u,x} - V_u g_2\right)\left(c_y + \frac{d}{2} - c_{AD}\right)}{J_{cx}} \tag{4}$$

$$v_{u(B)} = \frac{V_u}{A_c} - \frac{\gamma_x\left(M_{u,y} - V_u g_1\right)\left(c_x + \frac{d}{2} - c_{AB}\right)}{J_{cy}} + \frac{\gamma_y\left(M_{u,x} - V_u g_2\right)c_{AD}}{J_{cx}} \tag{5}$$

$$A_c = \left(c_x + c_y + d\right)d \tag{6}$$

$$c_{AB} = \frac{\left(c_x + \frac{d}{2}\right)^2 d}{2A_c} \tag{7}$$

$$c_{AD} = \frac{\left(c_y + \frac{d}{2}\right)^2 d}{2A_c} \tag{8}$$

$$J_{cx} = \frac{d\left(c_y + \frac{d}{2}\right)^3}{12} + \frac{\left(c_y + \frac{d}{2}\right)d^3}{12} + \left(c_x + \frac{d}{2}\right)dc_{AD}^2 + \left(c_y + \frac{d}{2}\right)d\left(\frac{c_y + \frac{d}{2}}{2} - c_{AD}\right)^2 \tag{9}$$

$$J_{cy} = \frac{d\left(c_x + \frac{d}{2}\right)^3}{12} + \frac{\left(c_x + \frac{d}{2}\right)d^3}{12} + \left(c_y + \frac{d}{2}\right)dc_{AB}^2 + \left(c_x + \frac{d}{2}\right)d\left(\frac{c_x + \frac{d}{2}}{2} - c_{AB}\right)^2 \tag{10}$$

where V_u is the design direct shear; A_c is the area of the critical section; $M_{u,x}$ and $M_{u,y}$ are the design unbalanced moments about the x-axis and y-axis, respectively (in this paper, x-axis refers to E-W direction, y-axis refers to N-S direction); J_{cx} and J_{cy} are the polar moment of inertia of the whole critical section with respect to the axes of x and y, respectively; and other definitions of g_1, g_2, c_{AB}, and c_{CD} are shown in Fig. 12.

Stresses (v_u) were calculated based on Eq. (1) to (10) and using mixed data points of V_u, $M_{u,x}$, and $M_{u,y}$ (Table 1) from experiments and simulations. Note that some data required to perform the calculation are not accessible from the experiments. For example, the experimental column reaction plots are not legible; thus, they were instead read from numerical simulations. These factors, however, make small contributions to v_u and the differences between the experiments and simulations should be small. These v_u values are compared with those directly obtained from numerical simulations—that is, the averages of five layers' numerical shear stresses along the slab thickness at specified locations (Fig. 13).

ACI 318-11, Section 11.11.2.2, defines the punching shear strength of an interior PT slab-column connection as

$$V_c = \left(\beta_p \lambda \sqrt{f_c'} + 0.3 f_{pc}\right)b_o d + V_p \tag{11}$$

where β_p is the smaller of 3.5 and ($\alpha_s d/b_o$ + 1.5) if f_c' is in psi; β_p is the smaller of 0.29 and 0.083 ($\alpha_s d/b_o$ + 1.5) if f_c' is in MPa; α_s = 40, 30, and 20 for interior,

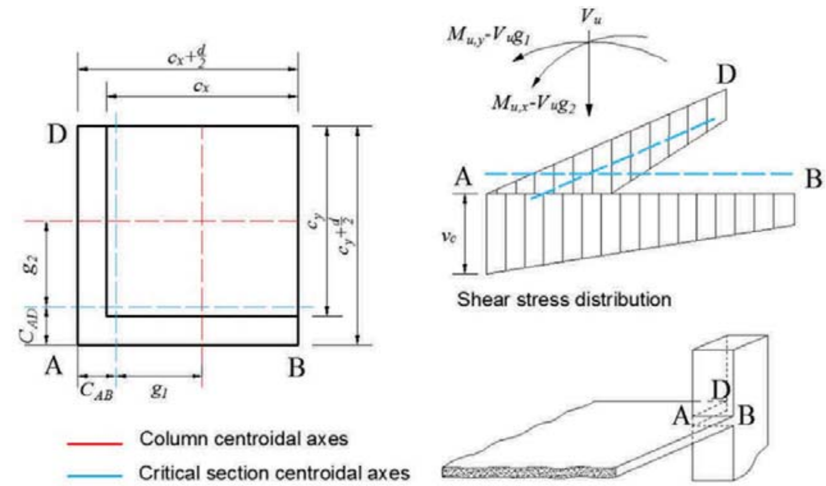

Fig. 12—Symbols and notation associated with eccentric shear-stress model (B: west corner; A: front corner; D: south corner).

exterior, and corner connections, respectively; λ is the lightweight concrete modification factor ($\lambda = 1$ for PT slabs with normalweight concrete); b_o is the perimeter of the assumed critical section; d is the slab effective depth; f_{pc} is the average compressive stress of concrete due to the effective post-tensioning force exerting on the full slab section; and V_p is the vertical component of all effective post-tensioning forces going through the critical section. The V_p term is approximately neglected in the study, as the tendon profile was relatively straight with almost zero eccentricity in the tested corner connection. Recall that Eq. (11) is not permitted if ACI 318-11, Sections 11.11.2.2(a), (b), and (c) are not satisfied. If the limits are not satisfied, Section 11.11.2.1 shall apply, which states that V_c shall be the smallest of Eq. (12) through (14).

$$V_c = \left(2 + \frac{4}{\beta}\right)\lambda\sqrt{f_c'}b_o d$$
$$V_c = 0.17\left(1 + \frac{2}{\beta}\right)\lambda\sqrt{f_c'}b_o d \quad \text{(SI)} \qquad (12)$$

where β is the ratio of the long side to short side of the column, concentrated load, or reaction area.

$$V_c = \left(\frac{a_s d}{b_o} + 2\right)\lambda\sqrt{f_c'}b_o d$$
$$V_c = 0.083\left(\frac{a_s d}{b_o} + 2\right)\lambda\sqrt{f_c'}b_o d \quad \text{(SI)} \qquad (13)$$

Here, a_s is 40 for interior columns, 30 for edge columns, and 20 for corner columns.

$$V_c = 4\lambda\sqrt{f_c'}b_o d$$
$$V_c = 0.33\lambda\sqrt{f_c'}b_o d \quad \text{(SI)} \qquad (14)$$

The specimens tested by Moehle et al. (1994) do not satisfy limits (a) and (b), which implies that the punching shear strength of these corner connections should be calculated using Eq. (12) through (14). These equations are equivalent to those of reinforced concrete slab-column connections without post-tensioning. ACI 318-11, Commentary R11.11.2.2, states that the prestress is not fully effective around the perimeter of the critical section near the slab edge; therefore, the prestressing effect is not taken into account calculating the shear capacity. Previous research on the four-panel PT flat plate (Gardner and Kallage 1998), however, did reveal that shear capacity increases, even if the critical section is near the slab edge. The current study is in agreement with the previous research finding, as described in the following paragraph.

Table 1 summarizes the stress calculations at experimental punching shear failure or possible punching failure points for simulations of c1a, c1b, c2a, and c2b. The notations of c1a', c1b', c2a', and c2b' represent the points at the ends of N-S lateral loading for c1a, c1b, c2a, and c2b simulations, respectively. The largest shear stress is marked for each case and compared with the shear-stress capacity v_{c1} and v_{c2}, as per ACI 318-11, Sections 11.12.2.1 (Eq. (12) to (14)) and 11.12.2.2 (Eq. (11)), respectively.

Table 1(a)—Summary of shear stresses calculated from different methods at various loading stages for simulations of c1a, c1b, c2a, and c2b

At punching failure or possible experimental failure points		V_u, lb (N)	$M_{u,x}$, in.-lb (N-m)	$M_{y,x}$, in.-lb (N-m)	Front	South	West	Front*	South*	West*	v_{c1}, psi (kPa)	v_{c2}, psi (kPa)	v_u/v_{c1}	Maximum shear stress/v_{c2}	
					γ_v = 0.4, psi (kPa)			γ_v = 0.3, psi (kPa)						γ_v = 0.4	γ_v = 0.3
c1a	FEA	NA			257 (1772)	82 (565)	−104 (−717)	257 (1772)	82 (565)	−104 (−717)	336 (2317)	307 (2117)	0.32	Front/v_{c2}	Front*/v_{c2}
	FEA (maximum)				258 (1772)	−516 (−3558)	−402 (−2772)	258 (1779)	−516 (−3558)	−402 (−2772)				—	—
	Method 1	5766‡ (25,648)	80,614‡ (9108)	91,888‡ (10,382)	371† (2558)	−81 (−558)	−158 (−1089)	306† (2110)	−33 (−228)	−92 (−634)				121%	100%
	Method 2	5766‡ (25,648)	89,089‡‡ (10,066)	115,064‡‡ (13,000)	432† (2979)	−81 (−558)	−263 (−1813)	351† (2420)	−34 (−234)	−170 (−1172)				141%	114%
c1a’	FEA	NA			179 (1234)	−516 (−3558)	−181 (−1248)	179 (1234)	−516 (−3558)	−181 (−1248)	336 (2317)	307 (2117)	0.28	South/v_{c2}	South*/v_{c2}
	FEA (maximum)				193 (1331)	−516 (−3558)	−402 (−2772)	193 (1331)	−516 (−3558)	−402 (−2772)				—	—
	Method 1	4977‡ (22,139)	131,638‡ (14,873)	9038‡ (1021)	305 (2103)	−529† (−3647)	347 (2392)	252 (1737)	−373† (−2572)	284 (1958)				172%	121%
	Method 2	4977‡ (22,139)	131,170‡‡ (14,820)	9038‡ (1021)	304 (2096)	−526† (−3627)	346 (2386)	251 (1731)	−371† (−2558)	283 (1951)				171%	121%
c1b	FEA	NA			112 (772)	245 (1689)	−85 (−586)	112 (772)	245 (1689)	−85 (−586)	336 (2317)	307 (2117)	0.38	Front/v_{c2}	Front*/v_{c2}
	FEA (maximum)				218 (1503)	−583 (−4020)	−402 (−2772)	218 (1503)	−583 (−4020)	−402 (−2772)				—	—
	Method 1	6816‡ (30,319)	77,841‡ (8795)	122,636‡ (13,856)	432† (2979)	23 (159)	−293 (−2020)	357† (2461)	49 (338)	−188 (−1296)				141%	116%
	Method 2	6816‡ (30,319)	84,393‡‡ (9535)	95,903‡‡ (10,836)	394† (2717)	−63 (−434)	−142 (−979)	328† (2261)	−15 (−103)	−74 (−510)				128%	107%
c1b’	FEA	NA			213 (1469)	−214 (−1475)	−34 (−234)	213 (1469)	−214 (−1475)	−34 (−234)	336 (2317)	307 (2117)	0.32	South/v_{c2}	South*/v_{c2}
	FEA (maximum)				218 (1503)	−583 (−4020)	−402 (−2772)	218 (1503)	−583 (−4020)	−402 (−2772)				—	—
	Method 1	5643‡ (25,101)	161,898‡ (18,292)	−7‡ (−1)	350 (2413)	−685† (−4723)	471 (3247)	289 (1993)	−487† (−3558)	380 (2620)				223%	159%
	Method 2	5643‡ (25,101)	146,700‡‡ (16,575)	−7‡ (−1)	321 (2213)	−606† (−4178)	442 (3047)	268 (1848)	−428† (−2951)	358 (2468)				197%	139%

‡Value from FEA; ‡‡Value from experiment; †Governing stress.

Notes: Units in lb-in. (N-m); $v_{c1} = 3.5\sqrt{f_c'} + 0.3f_{pc}$ ($v_{c1} = 0.29\sqrt{f_c'} + 0.3f_{pc}$); $v_{c2} = 4\sqrt{f_c'}$ ($0.33\sqrt{f_c'}$); NA is not available.

Table 1(b)

At punching failure or possible experimental failure points		V_u, lb (N)	$M_{u,x}$, in.-lb (N-m)	$M_{y,x}$, in.-lb (N-m)	Front	South	West	Front*	South*	West*	v_{c1}, psi (kPa)	v_{c2}, psi (kPa)	v_u/v_{c1}	Maximum shear stress/v_{c2}	
					γ_v = 0.4, psi (kPa)			γ_v = 0.3, psi (kPa)						γ_v = 0.4	γ_v = 0.3
c2a	FEA	NA			172 (1186)	132 (910)	–94 (–648)	172 (1186)	132 (910)	–94 (–648)	336 (2317)	313 (2158)	0.32	Front/v_{c2}	Front*/v_{c2}
	FEA (maximum)				200 (1379)	–545 (3758)	–361 (–2489)	200 (1389)	–545 (–3758)	–361 (–2489)				—	—
	Method 1	5778‡ (25,702)	87,796‡ (9920)	88,593‡ (10,010)	379† (2613)	–124 (–855)	–127 (–876)	311† (2144)	–66 (–455)	–68 (–469)				121%	99%
	Method 2	5778‡ (25,702)	111,507‡‡ (12,599)	119,072‡‡ (13,453)	482† (3323)	–191 (–1317)	–241 (–1662)	389† (2682)	–116 (–800)	–153 (–1055)				154%	124%
c2a'	FEA	NA			175 (1207)	–542 (–3737)	–91 (–627)	175 (1207)	–542 (–3737)	–91 (–627)	336 (2317)	313 (2158)	0.28	South/v_{c2}	South*/v_{c2}
	FEA (maximum)				183 (1262)	–545 (–3758)	–361 (–2489)	183 (1262)	–545 (–3758)	–361 (–2489)				—	—
	Method 1	4946‡ (22,001)	143,436‡ (16,206)	369‡ (42)	311 (2144)	–608† (–4192)	414 (2854)	256 (1765)	–433† (–2985)	334 (2303)				194%	138%
	Method 2	4946‡ (22,001)	148,954‡‡ (16,830)	369‡ (42)	321 (2213)	–637† (–4392)	424 (2923)	264 (1820)	–454† (–3130)	342 (2358)				203%	145%
c2b	FEA	NA			164 (1131)	258 (1779)	–164 (–1131)	164 (1131)	258 (1779)	–164 (–1131)	336 (2317)	313 (2158)	0.36	Front/v_{c2}	Front*/v_{c2}
	FEA (maximum)				223 (1538)	–552 (–3806)	–361 (–2489)	223 (1538)	–552 (–3806)	–361 (–2489)				—	—
	Method 1	6395‡ (28,446)	84,882‡ (9590)	116,584‡ (13,172)	431† (2972)	–38 (–262)	–261 (–1800)	354† (2441)	2 (14)	–165 (–1138)				138%	113%
	Method 2	6395‡ (28,446)	83,015‡‡ (9379)	129,717‡‡ (14,656)	453† (3123)	–3 (–21)	–332 (–2289)	370† (2551)	28 (193)	–219 (–1510)				145%	118%
c2b'	FEA	NA			214 (1475)	–244 (–1682)	29 (200)	214 (1475)	–244 (–1682)	29 (200)	336 (2317)	313 (2158)	0.29	South/v_{c2}	South*/v_{c2}
	FEA (maximum)				220 (1517)	–552 (–3806)	–361 (–2489)	220 (1517)	–552 (–3806)	–361 (–2489)				—	—
	Method 1	5200‡ (23,131)	165,440‡ (18,692)	–6531‡ (–738)	341 (2351)	–729† (–5026)	499 (3440)	280 (1931)	–522† (–3599)	399 (2751)				233%	167%
	Method 2	5200‡ (23,131)	146,387‡‡ (16,540)	–6531‡ (–738)	305 (2103)	–629† (–4337)	463 (3192)	253 (1744)	–448† (–3089)	371 (2558)				201%	143%

‡Value from FEA; ‡‡Value from experiment; †Governing stress.

Notes: Units in lb-in. (N-m); $v_{c1} = 3.5\sqrt{f'_c} + 0.3f_{pc}$ ($v_{c1} = 0.29\sqrt{f'_c} + 0.3f_{pc}$); $v_{c2} = 4\sqrt{f'_c}$ ($0.33\sqrt{f'_c}$); NA is not available.

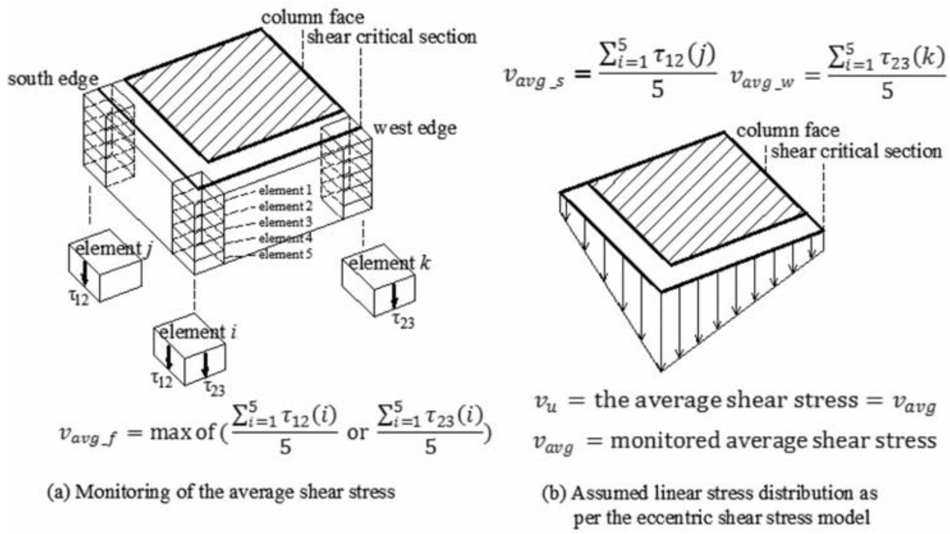

Fig. 13—Monitoring of direct and eccentric (torsional) shear stresses associated with eccentric shear-stress model.

In Table 1, "FEA" and "FEA(max)" represent the current and maximum shear-stress readings, respectively, during the simulation. The large discrepancy between "FEA" and "FEA(max)" indicates the fact that the maximum numerical shear stress might not occur right at the ends of lateral loadings. Figures 14(a) and (b) reveal that the maximum shear stress actually occurred at the south corner during the N-S lateral loading in all the conducted simulations. The maximum shear stress exceeded the capacity suggested by Eq. (11), except the front corner of c2b and c2b-2.5, implying that Eq. (11) appears to also be conservative for corner PT connections. Based on the numerical data, several critical data points other than at the ends of lateral loadings are also included in Table 1.

The very large ratio of maximum shear stress to v_{c2} indicates that the shear stress predicted by the eccentric shear-stress model underestimates actual punching shear capacity (note that the stress calculated from Method 2 in Table 1 is mostly based on the experimental data). Given the fact that the actual experimental punching failures of Specimens C1 and C2 did occur after reaching the maximum shear stress, either the eccentric shear-stress model and/or the punching shear capacity prediction is overly conservative. As a comparison, stresses calculated based on a reduced unbalanced moment transfer factor (γ_v = 0.3) are also included in Table 1. Even with the reduced unbalanced moment transfer factor, the maximum shear stresses are still larger than v_{c2} in most cases. Table 2 summarizes the simulations of c1a-2.5, c1b-2.5, c2a-2.5,

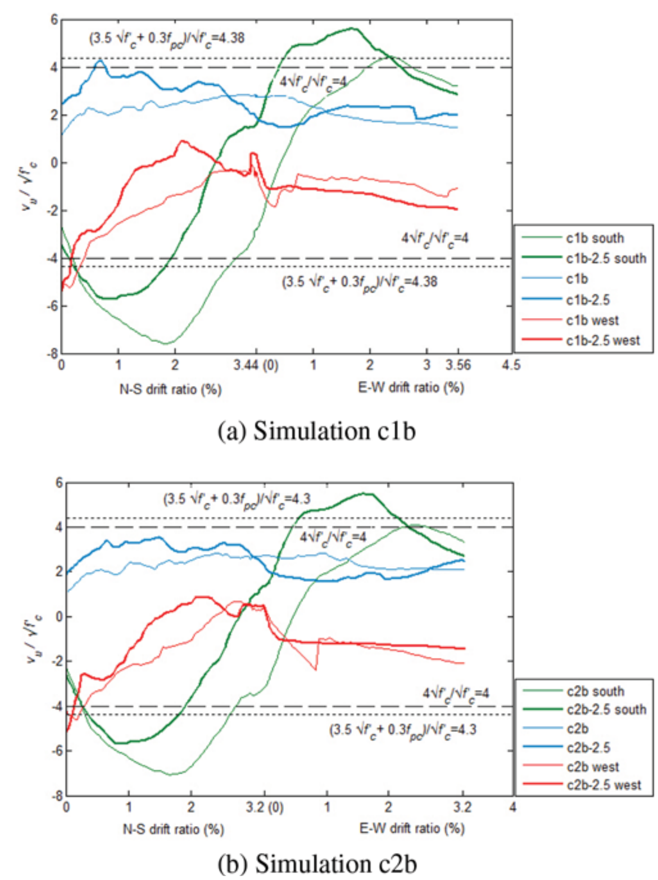

Fig. 14—Normalized numerical shear stress versus drift ratio at three critical locations (from numerical simulations of c1b, c1b-2.5, c2b, and c2b-2.5). (Note: f'_c in units of psi.)

Table 2(a)—Summary of shear stresses calculated from different methods at various loading stages for simulations of c1a-2.5, c1b-2.5, c2a-2.5, and c2b-2.5

At punching failure or possible experimental failure points		V_u, lb (N)	$M_{u,x}$, in.-lb (N-m)	$M_{y,x}$, in.-lb (N-m)	Front	South	West	Front*	South*	West*	v_{c1}, psi (kPa)	v_{c2}, psi (kPa)	$\frac{v_u}{v_{c1}}$	Maximum shear stress/v_{c2}	
					$\gamma_v = 0.4$, psi (kPa)			$\gamma_v = 0.3$, psi (kPa)						$\gamma_v = 0.4$	$\gamma_v = 0.3$
c1a-2.5	FEA	NA			266 (1834)	165 (1138)	−74 (−510)	266 (1834)	165 (1138)	−74 (−510)	336 (2317)	307 (2117)	0.49	Front/v_{c2}	Front*/v_{c2}
	FEA (maximum)				328 (2261)	−443 (−3054)	−418 (−2882)	328 (2261)	−443 (−3054)	−418 (−2882)				—	—
	Method 1	8732 (38,842)	99,635 (11,257)	105,246 (11,891)	455† (3137)	−69 (−476)	−106 (−731)	382† (2634)	−11 (−76)	−38 (−262)				148%	125%
c1a'-2.5	FEA	NA			295 (2034)	−418 (−2882)	−47 (−324)	295 (2034)	−418 (−2882)	−47 (−324)	336 (2317)	307 (2117)	0.45	South/v_{c2}	South*/v_{c2}
	FEA (maximum)				328 (2261)	−443 (−3054)	−418 (−2882)	328 (2261)	−443 (−3054)	−418 (−2882)				—	—
	Method 1	8103 (36,044)	151,654 (17,135)	28,140 (3179)	403 (2779)	507† (3496)	376 (2592)	340 (2344)	−342† (−2358)	320 (2206)				165%	111%
c1b-2.5	FEA	NA			153 (1055)	218 (1503)	−151 (−1041)	153 (1055)	218 (1503)	−151 (−1041)	336 (2317)	307 (2117)	0.49	Front/v_{c2}	Front*/v_{c2}
	FEA (maximum)				328 (2261)	−441 (−3041)	−418 (−2882)	328 (2261)	−441 (−3041)	−418 (−2882)				—	—
	Method 1	8805 (39,167)	47,583 (5376)	126,484 (14,291)	397† (2737)	246 (1696)	−314 (−2165)	339† (2337)	226 (1538)	−194 (−1338)				129%	110%
c1b'-2.5	FEA	NA			144 (993)	123 (848)	24 (165)	144 (993)	123 (848)	24 (165)	336 (2317)	307 (2117)	0.45	Front/v_{c2}	Front*/v_{c2}
	FEA (maximum)				328 (2261)	−441 (−3041)	−418 (−2882)	328 (2261)	−441 (−3041)	−418 (−2882)				—	—
	Method 1	8014 (35,648)	121,976 (13,781)	43,242 (4886)	374† (2579)	−279 (−1924)	248 (1710)	318† (2293)	−171 (−1179)	224 (1544)				122%	104%

†Governing stress.

Notes: Units in lb-in. (N-m); $v_{c1} = 3.5\sqrt{f_c'} + 0.3f_{pc}$ ($v_{c1} = 0.29\sqrt{f_c'} + 0.3f_{pc}$); $v_{c2} = 4\sqrt{f_c'}$ ($0.33\sqrt{f_c'}$); NA is not available.

Table 2(b)

At punching failure or possible experimental failure points		V_u, lb (N)	$M_{u,x}$, in.-lb (N-m)	$M_{y,x}$, in.-lb (N-m)	Front	South	West	Front*	South*	West*	v_{c1}, psi (kPa)	v_{c2}, psi (kPa)	$\frac{v_u}{v_{c1}}$	Maximum shear stress/v_{c2}	
					$\gamma_v = 0.4$, psi (kPa)			$\gamma_v = 0.3$, psi (kPa)						$\gamma_v = 0.4$	$\gamma_v = 0.3$
c2a-2.5	FEA	NA			233 (1606)	228 (1572)	−86 (−593)	233 (1538)	228 (1572)	−86 (−593)	336 (2317)	313 (2158)	0.48	Front/v_{c2}	Front*/v_{c2}
	FEA (maximum)				283 (1951)	−446 (−3075)	−401 (−2765)	283 (1951)	−446 (−3075)	−401 (−2765)				—	—
	Method 1	8470 (37,676)	103,285 (11,670)	99,775 (11,273)	450† (3103)	−106 (−731)	−78 (−538)	377† (2599)	−40 (−276)	−19 (−131)				144%	120%
c2a-2.5'	FEA	NA			239 (1648)	−366 (−2523)	19 (131)	239 (1648)	−366 (−2523)	19 (131)	336 (2317)	313 (2158)	0.44	South/v_{c2}	South*/v_{c2}
	FEA (maximum)				283 (1951)	−446 (−3075)	−401 (−2765)	283 (1951)	−446 (−3075)	−401 (−2765)				—	—
	Method 1	7765 (34,540)	160,048 (18,083)	14,749 (1666)	391 (2696)	−586† (−4040)	452 (3116)	330 (2275)	−403† (−2779)	375 (2586)				187%	129%
c2b-2.5	FEA	NA			196 (1351)	210 (1448)	−116 (−800)	196 (1351)	210 (1448)	−116 (−800)	336 (2317)	313 (2158)	0.47	Front/v_{c2}	Front*/v_{c2}
	FEA (maximum)				276 (1903)	−446 (−3075)	−401 (−2765)	276 (1903)	−446 (−3075)	−401 (−2765)				—	—
	Method 1	8426 (37,481)	58,752 (6638)	122,959 (13,893)	409† (2820)	170 (1172)	−285 (−1965)	346† (2386)	167 (1151)	−174 (−1200)				130%	111%
c2b-2.5'	FEA	NA			173 (1193)	108 (745)	23 (159)	173 (1193)	108 (745)	23 (159)	336 (2317)	313 (2158)	0.44	South/v_{c2}	Front*/v_{c2}
	FEA (maximum)				276 (1903)	−446 (−3075)	−401 (−2765)	276 (1903)	−446 (−3075)	−401 (−2765)				—	—
	Method 1	7762 (34,527)	134,594 (15,207)	37,582 (4246)	386 (2661)	−409† (−2820)	284 (1958)	326† (2248)	−270 (−1862)	250 (1724)				131%	104%

†Governing stress.

Notes: Units in lb-in. (N-m); $v_{c1} = 3.5\sqrt{f'_c} + 0.3f_{pc}$ ($v_{c1} = 0.29\sqrt{f'_c} + 0.3f_{pc}$); $v_{c2} = 4\sqrt{f'_c}$ ($0.33\sqrt{f'_c}$); NA is not available.

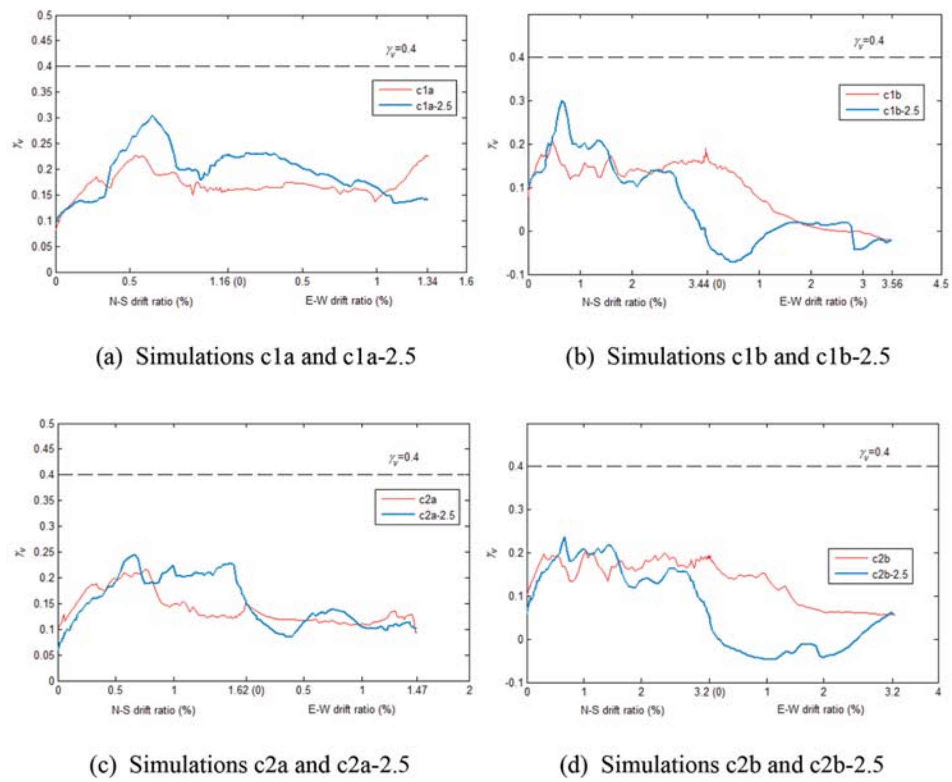

(a) Simulations c1a and c1a-2.5

(b) Simulations c1b and c1b-2.5

(c) Simulations c2a and c2a-2.5

(d) Simulations c2b and c2b-2.5

Fig. 15—Unbalanced moment transfer ratio at front corner of each simulation.

and c2b-2.5, and shows the same results as Table 1 suggests. This indicates that the nominal punching shear strength on the basis of Eq. (12) to (14) is not representative of the actual shear strength of corner PT connections.

It would be more proper to evaluate the eccentric shear-stress model when the shear stress reaches the peak in the critical section. Table 3 shows the evaluations made at those data points, where the "FEA" and "FEA(max)" are the same. Nevertheless, considering that the upward initial shear stresses at the south and west corners are not considered in the eccentric shear-stress model, the actual shear stresses would be much higher than the numerical shear stresses. Therefore, the results still yield the same conclusion that either the eccentric shear-stress model or the shear-stress capacity as per ACI 318-11 (Section 11.12.2.1) is conservative. The next subsection discusses more about unbalanced moment transfer ratio (γ_v).

Assessment of unbalanced moment transfer factor

The assessment of γ_v is accomplished by substituting numerical shear stress v_u into Eq. (3). This assessment is purely based on numerical results. Because the upward initial shear stresses are very large at the south corner and west corner due to prestress, only the front corner stress (at Point A in Fig. 12) is evaluated in this study. Figure 15 shows the derived γ_v from the method described previously. All γ_v values show a similar pattern. They are always smaller than 0.3 and tend to decrease as the drift ratios increase. This is consistent with the conclusion drawn from the preceding subsection (that is, conclusions about the values in Tables 1 to 3), as well as the companion PT edge connection study previously conducted by the same authors (Kang and Huang 2012). The decreasing γ_v against the drift is reasonable because the connection region is no longer rigidly elastic as the cracks progress. Subsequently, torsional resistance would be compromised with the yield of bonded steel, leading to the reduction of torsional transfer of unbalanced moment. Therefore, a conclusion can be drawn together with the analysis of the preceding subsection that a reduction of γ_v to 0.3 (or possibly up to 0.2) is suggested for the punching shear design of a corner PT slab-column connection. Even though the analyses based on both the experimental and numerical data lead to the same conclusion as

Table 3—Summary of shear stresses calculated from different methods at various loading stages for c1b, c1b-2.5, c2b, and c2b-2.5

At punching failure or possible experimental failure points		V_u, lb (N)	$M_{u,x}$, in.-lb (N-m)	$M_{y,x}$, in.-lb (N-m)	Front	South	West	Front*	South*	West*	v_{c1}, psi (kPa)	v_{c2}, psi (kPa)	$\frac{v_u}{v_{c1}}$	Maximum shear stress/v_{c2}
					$\gamma_v = 0.4$, psi (kPa)			$\gamma_v = 0.3$, psi (kPa)						$\gamma_v = 0.4$
c1b	FEA	NA			180 (1241)	–583 (–4020)	–113 (–779)	180 (1241)	–583 (–4020)	–113 (–779)	336 (2317)	307 (2117)	0.49	South/v_{c2}
	FEA (maximum)				198 (1365)	–583 (–4020)	–402 (–2772)	198 (1365)	–583 (–4020)	–402 (–2772)				—
	Method 1	5069 (22,548)	137,729 (15,561)	6560 (741)	347 (2392)	–665† (–4585)	449 (3096)	286 (1972)	–473† (–3261)	362 (2496)				217%
c1b-2.5	FEA	NA			271 (1868)	–441 (–3041)	–167 (–1151)	271 (1868)	–441 (–3041)	–167 (–1151)	336 (2317)	307 (2117)	0.45	South/v_{c2}
	FEA (maximum)				328 (2261)	–441 (–3041)	–418 (–2882)	328 (2261)	–441 (–3041)	–418 (–2882)				—
	Method 1	7999 (35,581)	145,276 (16,414)	29,269 (3307)	392 (2703)	–453† (–3123)	329 (2268)	331† (2282)	–302 (–2082)	284 (1958)				147%
c2b	FEA	NA			186 (1282)	–552 (–3806)	–102 (–703)	186 (1282)	–552 (–3806)	–102 (–703)	336 (2317)	307 (2117)	0.50	South/v_{c2}
	FEA (maximum)				196 (1351)	–552 (–3806)	–361 (–2489)	196 (1351)	–552 (–3806)	–361 (–2489)				—
	Method 1	4434 (19,723)	115,002 (12,993)	11,431 (1292)	315 (2172)	–631† (–4351)	439 (3027)	260 (1793)	–449† (–3096)	353 (2434)				206%
c2b-2.5	FEA	NA			258 (1779)	–446 (–3075)	–159 (–1096)	258 (1779)	–446 (–3075)	–159 (–1096)	336 (2317)	307 (2117)	0.45	South/v_{c2}
	FEA (maximum)				266 (1834)	–446 (–3075)	–401 (–2765)	266 (1834)	–446 (–3075)	–401 (–2765)				—
	Method 1	7404 (32,935)	137,962 (15,588)	27,441 (3100)	374 (2579)	–468† (–3227)	344 (2372)	316† (2179)	–316 (–2179)	293 (2020)				153%

†Governing stress.

Notes: Units in lb-in. (N-m); $v_{c1} = 3.5\sqrt{f'_c} + 0.3f_{pc}$ ($v_{c1} = 0.29\sqrt{f'_c} + 0.3f_{pc}$); $v_{c2} = 4\sqrt{f'_c}$ ($0.33\sqrt{f'_c}$); NA is not available.

in this study, more investigations of corner PT slab-column connections are of great need for further understanding the punching shear-failure mechanism.

SUMMARY AND CONCLUSIONS

The previously proposed finite element modeling schemes dealing with unbonded PT structures have been used in this study to investigate ACI 318-11 punching shear provisions applying to corner PT slab-column connections. Two corner specimens tested by Moehle et al. (1994) were modeled. Reasonable agreements are achieved between the numerical simulations and experiments. Based on the investigation, the following conclusions can be drawn:

1. The initial shear stress due to prestress could be considered in the ACI 318-11 punching shear provisions, particularly in the direction of banded post-tensioning tendons.

2. The shear-stress value and distribution on the critical section and the shear-stress variation against the drift reasonably agree with the shear-transfer mechanism proposed by the eccentric shear-stress model. However, as the connection damage progresses, the degree of eccentric shear transfer of unbalanced moment seems to decrease. The plot of γ_v versus the drift ratio yields the same conclusion that γ_v never exceeded 0.3 and decreased as the cracks proceeded. A reduction of γ_v to 0.3 or possibly 0.2 could be considered for the design of corner PT slab-column connections.

3. The current punching shear provisions are too conservative regarding corner PT slab-column corner connections. Evidence has suggested that design shear strength, even with the reduced unbalanced moment transfer ratio γ_v, still led to conservative design. The maximum shear stress taken directly from the numerical model is greater than both the ACI 318 capacities with and without consideration of the prestressing effect. Again, two potential reasons are that: 1) the upward initial shear stresses are not considered in the eccentric shear-stress model; and 2) the shear capacity equation, including PT contribution, is not allowed by ACI 318-11. However, more experimental investigations are needed to further quantify verdicts drawn in this study and to improve the design guidelines of corner PT slab-column connections in ACI 318.

ACKNOWLEDGMENTS

This work was supported by the National Research Foundation of Korea (NRF) grant funded by the Korea government (MEST) (No. 2012-005905). The authors also thank partial supports from the University of Oklahoma and the Engineering Research Institute at Seoul National University. The authors would like to acknowledge PTI Building Design Committee members R. Ahmed, J. Ales, B. Allred, A. Baxi, M. Cuadra, C. Hayek, J. Hirsch, D. Kline, C. Kopczynski, and M. Vejvoda for their active discussion concerning the design of post-tensioned buildings during committee meetings and conference calls. The views expressed are those of the authors and do not necessarily represent those of the sponsor or discussers.

REFERENCES

ACI Committee 318, 2011, "Building Code Requirements for Structural Concrete (ACI 318-11) and Commentary," American Concrete Institute, Farmington Hills, MI, 503 pp.

Brotchie, J. F., and Beresford, F. D., 1967, "Experimental Study of a Prestressed Concrete Flat Plate Structure," *Civil Engineering Transactions,* Institution of Engineers, Sydney, Australia, Oct., pp. 267-282.

Burns, N. H., and Hemakom, R., 1977, "Test of Scale Model Post-Tensioned Flat Plate," *Proceedings*, ASCE, V. 103, No. ST6, June, pp. 1237-1255.

Burns, N. H., and Hemakom, R., 1985, "Test of Flat Plate with Banded Tendons," *Proceedings*, ASCE, V. 111, No. 9, Sept., pp. 1899-1915.

Gamble, W. L., 1964, "An Experimental Investigation of the Strength and Behavior of a Prestressed Concrete Flat Plate," *Report* T80-9, Division of Building Research, Commonwealth (of Australia) Scientific and Industrial Research Organization, Melbourne, Australia.

Garnder, N. J., and Kallage, M. R., 1998, "Punching Shear Strength of Continuous Post-Tensioned Concrete Flat Plates," *ACI Materials Journal*, V. 95, No. 3, May-June, pp. 272-283.

Huang, Y.; Kang, T. H.-K.; Ramseyer, C.; and Rha, C., 2010, "Background to Multi-Scale Modeling of Unbonded Post-Tensioned Concrete Structures," *International Journal of Theoretical and Applied Multiscale Mechanics*, V. 1, No. 3, pp. 219-235.

Huang, Y., 2012, "Finite Element Method for Post-Tensioned Prestressed Concrete Structures," PhD thesis, School of Civil Engineering and Environmental Science, University of Oklahoma, Norman, OK, 326 pp.

Kang, T. H.-K., and Huang, Y., 2012, "Nonlinear Finite Element Analyses of Unbonded Post-Tensioned Slab-Column Connections," *PTI JOURNAL*, V. 8, No. 1, July, pp. 4-19.

Kosut, G.; Burns, N.; and Winter, C., 1985, “Test of Four-Panel Post-Tensioned Flat Plate,” *Journal of Structural Engineering*, ASCE, V. 111, No. 9, Sept., pp. 1916-1929.

Martinez-Cruzado, J., 1993, “Experimental Study of Post-Tensioned Flat Plate Exterior Slab-Column Connections Subjected to Gravity and Biaxial Loading,” PhD thesis, Department of Civil Engineering, University of California, Berkeley, Berkeley, CA, 354 pp.

Moehle, J. P.; Martinez-Cruzado, J. A.; and Qaisrani, A., 1994, “Post-Tensioned Flat Plate Slab-Column Connections Subjected to Earthquake Loading,” *Proceedings, 5th National Conference on Earthquake Engineering, Earthquake Engineering Research Institute*, Chicago, IL, July, pp. 10-14.

Muspratt, M. A., 1969, “Behavior of a Prestressed Concrete Waffle Slab with Unbonded Tendons,” *ACI Journal*, V. 66, No. 12, Dec., pp. 1001-1004.

Odello, R. J., and Mehta, B. M., 1967, “Behavior of a Continuous Prestressed Concrete Slab with Drop Panels,” Graduate Student Report, Division of Structural Engineering and Structural Mechanics, University of California, Berkeley, Berkeley, CA.

Scordelis, A. C.; Lin, T. Y.; and Itaya, R., 1959, “Behavior of a Continuous Slab Prestressed in Two Directions,” *ACI Journal*, V. 56, No. 6, June, pp. 441-459.

PTI Fellow **Thomas H.-K. Kang** *is an Assistant Professor at Seoul National University, Seoul, Korea. Previously, he was an Assistant Professor at the University of Oklahoma, Norman, OK. He is a licensed professional engineer in California. He is a member of PTI Committee DC-20, Building Design. He received his BS from Seoul National University, and his PhD from the University of California (UCLA), Los Angeles, CA. His research interests include design and rehabilitation of post-tensioned buildings and systems.*

Yu Huang *is a Structural Engineer at Guard-All Building Solutions in Dallas, TX. Previously, he was a Graduate Research Assistant at the University of Oklahoma. He received his BS from ChongQing JiaoTong University, ChongQing, China, and his MS and PhD from the University of Oklahoma. His research interests include finite element analyses of post-tensioned prestressed concrete structures.*